Journal of Materials Chemistry A

Multimodal quantification of degradation pathways during extreme fast charging of lithium-ion batteries

Journal:	*Journal of Materials Chemistry A*
Manuscript ID	TA-ART-07-2022-005887.R1
Article Type:	Paper
Date Submitted by the Author:	11-Oct-2022
Complete List of Authors:	McShane, Eric; University of California Berkeley, Chemical and Biomolecular Engineering; Lawrence Berkeley National Laboratory, Energy Storage and Distributed Resources Division Paul, Partha; SLAC National Accelerator Laboratory; ESRF; The Henry Royce Institute Tanim, Tanvir; Idaho National Laboratory, Energy Storage and Electric Transportation Cao, Chuntian; Brookhaven National Laboratory, Computational Science Initiative Steinrück, Hans-Georg; Paderborn University, Department Chemie Thampy, Vivek; SLAC National Accelerator Laboratory Trask, Stephen; Argonne National Laboratory, Chemical Sciences and Engineering Division Dunlop, Alison; Argonne National Laboratory, Chemical Sciences and Engineering Division Jansen, Andrew; Argonne National Laboratory, Chemical Sciences and Engineering Division Dufek, Eric; Idaho National Laboratory, Energy Storage and Electric Transportation Toney, Michael; University of Colorado at Boulder, Chemical and Biological Engineering; University of Colorado at Boulder, Renewable and Sustainable Energy Institute (RASEI) Nelson Weker, Johanna L.; SLAC National Accelerator Laboratory McCloskey, Bryan; University of California Berkeley, Department of Chemical and Biomolecular Engineering; Lawrence Berkeley National Laboratory, Energy Storage and Distributed Resources Division

Journal Name

ARTICLE TYPE

Cite this: DOI: 00.0000/xxxxxxxxxx

Multimodal quantification of degradation pathways during extreme fast charging of lithium-ion batteries†

Eric J. McShane,[a*] Partha P. Paul,[b,c,d*] Tanvir R. Tanim,[e] Chuntian Cao,[f] Hans-Georg Steinrück,[g] Vivek Thampy,[b] Stephen E. Trask,[h] Alison R. Dunlop,[h] Andrew N. Jansen,[h] Eric J. Dufek,[e] Michael F. Toney,[i,j,‡] Johanna Nelson Weker,[b,‡] and Bryan D. McCloskey[a,‡]

Received Date
Accepted Date

DOI: 00.0000/xxxxxxxxxx

Enabling fast charging of Li-ion batteries will be a key step towards realizing the technology's full potential in electric vehicles. Currently, fast charging is limited by a variety of processes that reduce cell capacity upon extended cycling. Using a multimodal approach combining incremental capacity analysis (dQ/dV), high energy X-ray diffraction (HEXRD), and mass spectrometry titration (MST), we identify specific degradation mechanisms — including Li plating, dead Li_xC_6 formation, Li_2C_2 formation, solid carbonate solid-electrolyte interphase (SEI) deposition, and loss of positive electrode active material (LAM_{PE}) — that occur during extended fast charge cycling. We find that Li plating is the major source of capacity loss in cells cycled at 6C, while non-carbonate SEI species deposition on the graphite anode is the main source of capacity loss when cycled at 4C. We also study local degradative phenomena by examining specific ~1-5 cm^2 regions of the cells using HEXRD and MST. We find that plated Li is often collocated with dead Li_xC_6, Li_2C_2, and solid carbonate SEI species, and these additional species cumulatively account for ~20% of the capacity lost during 6C cycling. Finally, in a cell with an anomalously high amount of LAM_{PE} (quantified via dQ/dV), we find that regions of cathode degradation were accompanied by non-carbonate SEI products on the adjacent region of the anode. We postulate that this phenomenon arises due to crosstalk between the electrodes, wherein soluble electrolyte oxidation products formed at the delithiated cathode migrate to the graphite anode and are ultimately deposited on the graphite surface. This work demonstrates the utility of combining multiple characterization techniques to reveal a more holistic understanding of degradative phenomena that occur across multiple length scales during fast charge.

1 Introduction

Lithium-ion batteries (LIBs) hold promise to mitigate the deleterious effects of climate change by enabling the transition from

[a] Chemical and Biomolecular Engineering, University of California & Energy Storage and Distributed Resources Division, Lawrence Berkeley National Laboratory, Berkeley, CA 94720, USA.
[b] SLAC National Accelerator Laboratory, 2575 Sand Hill Road, Menlo Park, CA 94025. USA.
[c] ESRF – The European Synchrotron, 71 Ave. des Martyrs, Grenoble, 38000. France.
[d] Henry Royce Institute, Department of Materials, The University of Manchester, Manchester, M1 3BB. UK.
[e] Energy Storage and Electric Transportation Department, Energy and Environmental Science and Technology, Idaho National Laboratory, Idaho Falls, ID 83415. USA.
[f] Computational Science Initiative, Brookhaven National Laboratory, Upton, NY 11973, USA.
[g] Department Chemie, Universität Paderborn, Warburger Str. 100, Paderborn, 33098. Germany.
[h] Chemical Sciences and Engineering Division, Argonne National Laboratory, 9700 South Cass Avenue, Lemont, IL 60439, USA.
[i] Department of Chemical and Biological Engineering, University of Colorado, Boulder, CO 80309, USA.
[j] Renewable and Sustainable Energy Institute (RASEI), University of Colorado, Boulder, CO 80309, USA.
* These authors contributed equally to this
‡ Corresponding authors; e-mails: michael.toney@colorado.edu, jlnel-

internal combustion engine vehicles to electric vehicles (EVs), but key challenges must be resolved to unlock the full potential of the technology. Although the cost of LIBs has decreased dramatically over the last decade (~20% per year)[1], technological improvements to LIBs, such as improving the fast charge capability, will be necessary to hasten this transition going forward[2]. While EVs can be slowly charged with residential outlets with minimal capacity loss, long trips necessitate faster charging, which can be accompanied by substantial capacity loss[3]. For this reason, there is significant interest in designing extreme fast charge (XFC) capable LIBs, which can be charged to 80% capacity in ~10 minutes while retaining reasonable energy density[3].

A number of degradation processes occur across various length scales (from the cell scale to the atomic scale), which limit LIB performance during XFC cycling[4]. In general, XFC charging is associated with high overpotentials, which trigger pernicious side reactions at both electrodes and ultimately result in impedance rise and cell capacity fade[4]. In subsequent paragraphs, we introduce the primary degradation processes that have been shown to substantially contribute to capacity fade when fast charging batteries.

The most prominent of such side reactions, Li plating, occurs when Li^+ is reduced to Li metal on the graphite anode surface instead of intercalating between graphitic layers. Once plated, Li is prone to lose electronic contact with the graphite particle, thereby reducing the inventory of cyclable Li within the cell[5]. Additionally, Li metal is often collocated with electrochemically inactive lithiated graphite (Li_xC_6), which likely becomes dislodged from the bulk graphite electrode due to stresses imparted by the volumetric expansion of plated Li and expansion of the graphite particles themselves during charge[6–8]. Hereafter, we refer to irreversibly plated Li as "dead Li," and we refer to lithiated graphite which is no longer cyclable as "dead Li_xC_6."

Plated Li is also highly reactive with both the electrolyte (typically $LiPF_6$ in a blend of ethylene carbonate (EC) and linear carbonates[9], such as ethyl methyl carbonate (EMC)) and species present in the solid-electrolyte interphase (SEI) on graphite. The SEI is initially formed during the first few slow cycles (often called "formation cycles") after the battery is assembled, and it is comprised of electrolyte salt and solvent degradation products, including primarily lithium fluoride (LiF) and solid carbonates, such as lithium ethylene dicarbonate (LiEDC), lithium ethylene monocarbonate (LiEMC), and lithium carbonate (Li_2CO_3)[10–13]. The reaction of plated Li with the electrolyte is known to result in additional solid carbonate formation, and the reaction of plated Li with solid carbonate species initially present in the SEI is known to form lithium acetylide (Li_2C_2)[14,15]. These SEI species are often referred to as "inactive Li," as they cannot be oxidized upon battery discharge and therefore reduce the amount of cyclable Li within the cell. The LIB aging mode by which dead and inactive Li are created is referred to as "loss of lithium inventory," or LLI[16]. We note that electrolyte oxidation and the formation of a cathode-electrolyte interphase (CEI) can also be classified as LLI, and CEI formation begins to occur at ~4.1-4.2 V[17]. Although CEI formation was not directly quantified in this work, we propose that cathode-electrolyte interactions play a non-trivial role in a corner region of one particular cell, as will be discussed in Section 3.2.2.

In addition to LLI, loss of lattice sites for Li intercalation on the electrodes can also lead to capacity fade during fast charge. The cathode employed in this work, lithium nickel manganese cobalt oxide ($LiNi_{0.5}Mn_{0.3}Co_{0.2}O_2$, or NMC-532), is known to crack as it is being rapidly delithiated during fast charge, leading to capacity fade due to the loss of active sites for Li intercalation within the positive electrode[18–20]. This LIB aging mode is referred to as "loss of positive electrode active material," or LAM_{PE}[21]. We note that only cathode particle cracking which results in electronic isolation of cathode fragments would contribute to LAM_{PE}. Less severe cracking that does not induce electronically isolated particle fragments would instead manifest as an impedance rise in the cell. Regarding loss of negative electrode active material, we refer to electronically isolated lithiated graphite particles as dead Li_xC_6, and loss of delithiated graphite material was not explored in this work, as we found in a prior study that this aging mode occurs to a negligible extent in our tested cells[18].

The two major forms of capacity loss — LLI and LAM_{PE} — often both occur to varying extents within a cell, and they can be intricately tied to one another, making it challenging to discern their individual contributions to the capacity fade. For example, highly delithiated surfaces created upon cathode particle cracking (LAM_{PE}) can react with the electrolyte to form oxidized soluble species, which can in turn be reduced and deposited on the graphite anode[22–24]. Incremental capacity analysis (dQ/dV, described in Section 2.2) allows one to quantify the extent of both LLI and LAM_{PE} by fitting a simulated dQ/dV profile to the experimentally measured dQ/dV profile as the battery ages[19,25,26]. dQ/dV analysis is advantageous because it is easy to implement, as it only requires standard current and voltage data from cell cycling. However, while it provides an estimate of the relative contribution of LLI and LAM_{PE} to the *global* capacity fade of the cell, it does not provide spatially-resolved information about the chemical origin of capacity loss. This local information becomes especially important when studying degradation mechanisms during fast charge, as various recent studies have revealed the heterogeneous nature of degradation across cm^2 *local* regions of pouch cell electrodes during XFC cycling[7,27–29].

Thus, to supplement the *global* (electrode- and cell-scale) information from dQ/dV analysis, we utilize additional characterization techniques which provide *local*, chemically specific information about degradation processes. The first local technique we employ, in situ high energy X-ray diffraction (HEXRD), offers a millimeter-scale spatial resolution and can be used to quantify LiC_{12}, LiC_6, Li metal, and the average lithiation state of the NMC locally at the end of cycling[30]. The results of such HEXRD measurements on the four cells studied in this manuscript have also been discussed elsewhere[8,30]. In this work, we combine HEXRD measurements with mass spectrometry titration (MST) measurements (performed on ~1-5 cm^2 pieces of the extracted graphite

son@slac.stanford.edu, bmcclosk@berkeley.edu

† Electronic Supplementary Information (ESI) available. See DOI: 00/00.

electrodes after cycling), through which we quantify dead Li, dead Li_xC_6, and inactive Li (including both Li_2C_2 and solid carbonate SEI species)[14]. By correlating the titrated parts of electrodes to the appropriate location on the HEXRD maps of the full electrodes, we quantify the extent of *local* degradation mechanisms (including plated Li, dead Li_xC_6, Li_2C_2, and solid carbonate deposition) to complement the *global* dQ/dV analysis.

Capacity fade mechanisms that arise during XFC cycling have been thoroughly studied, but each has study has had certain limitations that we aim to bridge in this work. For example, prior work revealed that dead Li, solid carbonate SEI growth, and (to a lesser extent) Li_2C_2 deposition all contribute to capacity fade during XFC cycling in Li-graphite coin cells, but the same insights have not yet been extended to full pouch cells, and the spatial collocation of dead Li and SEI species across a full electrode has not yet been explored[14]. In a similar vein, degradation mechanisms that arise over the course of many fast charge cycles in full pouch cells have been elucidated using rest voltage signature analysis[31–33], dQ/dV analysis[34–38], and machine learning algorithms[39]. These studies showed that LLI contributes a significant portion of the lost capacity over XFC cycling, and LAM_{PE} plays a secondary yet non-trivial role[40]. However, the techniques in each study were necessarily applied only at the *global* cell scale, and information about *local* degradation mechanisms could not be ascertained[41]. Finally, previous HEXRD measurements on the same cells used in this work have uncovered trends regarding *local* degradation, such as the spatial collocation of dead Li and dead Li_xC_6, but these measurements were only conducted at the beginning and end of the 450 cycle fast charge procedure, and other degradation mechanisms, such as SEI growth, were not captured by the HEXRD measurements[8,30].

With these prior findings in mind, we address three major questions in this work. First, what is the *global* correlation between the amount of specific SEI components (solid carbonate SEI and Li_2C_2) and the amount of plated Li among four tested cells? Second, how do these *global* correlations manifest at the *local* scale? Finally, what is the role of *local* LAM_{PE}, and how can *local* (here cm^2 length scale) degradation at the cathode influence degradation processes at the anode? Using a unique combination of dQ/dV, MST, and HEXRD measurements, we address these questions and quantify the extent of specific degradation mechanisms that occur during prolonged fast charge cycling. The insights gleaned from this work can inspire novel electrolyte compositions, electrode architectures, and cell preparation procedures to minimize capacity loss during fast charging.

2 Materials and Methods

2.1 Pouch Cell Cycling

Four single-layer pouch cells, each of which underwent 450 XFC cycles, were studied in this work. These same four cells were also analyzed in previous work[8,29,30], but key details about the cells are repeated here for clarity. The cells were assembled in the Cell Analysis, Modeling, and Prototyping (CAMP) Facility and consisted of graphite anodes (3.0 mAh/cm^2, 34.5% porosity), nickel manganese cobalt oxide-532 ($LiNi_{0.5}Mn_{0.3}Co_{0.2}O_2$) cathodes (2.67 mAh/$cm^2$, 35.4% porosity), and Celgard 2320 separator wetted with 1.2 M $LiPF_6$ in 3:7 by weight ethylene carbonate:ethyl methyl carbonate electrolyte. Each anode had an area of 14.9 cm^2 and a thickness of 70 μm with a 10 μm Cu current collector, while each cathode had an area of 14.1 cm^2 with a thickness of 71 μm with a 20 μm Al current collector. The full composition of each electrode can be found in the ESI Section S1 †.

The formation protocol, described in depth elsewhere[8,42], consisted of three constant-current (CC) C/10 cycles followed by three CC C/2 cycles with 3.0 and 4.1 V cutoff voltages. After formation, each cell stack underwent 450 fast charge cycles at 30 °C with an applied cell pressure of ~15-30 kPa. The discharge protocol remained the same among all cells (a CC C/2 discharge from 4.1 V to 3.0 V), and three different charging protocols were studied:

1. **4C CCCV**: The cell was charged at constant current (CC) using a 4C rate until 4.1 V was reached, followed by a constant voltage (CV) hold at 4.1 V until 15 minutes of total charge time had elapsed.

2. **6C CCCV**: The cell was charged at 6C until 4.1 V was reached, followed by a CV hold at 4.1 V until until 10 minutes of total charge time had elapsed.

3. **6C 2-step**: The cell was charged at 6C until 4.1 V was reached, followed by a CC step at a lower rate. This lower rate was set as the theoretical rate required to fully charge the remaining capacity by the end of the full 10-minute charge. However, if 4.1 V was reached during this lower rate CC step, a CV hold at 4.1 V was used for the remainder of the 10-minute charge time[29].

The cycling protocols used in the four tested cells are summarized in Table 1. The nomenclature is consistent with that used in prior studies on the same cells[8,30].

Table 1 XFC charging protocols for all tested cells

Cell Name	XFC Charging Protocol
4C-a	4C CCCV
6C-a	6C CCCV
6C-b	6C 2-step
6C-c	6C 2-step

After every ~25 cycles, a CC C/20 reference performance test (RPT) cycle was conducted to determine the reversible cell capacity as a function of cycle number. The capacity losses for each cell over the 450 XFC cycles, as well as the cell capacities post-formation and post-XFC, are provided in ESI Section S2 †. After the final RPT (450^{th}) cycle (ending with a C/20 discharge to 3.0 V followed by a resting period of 1-3 months with no applied pressure), the cells were characterized with HEXRD. The respective results of such measurements are also reported in previous work[8,29,30]. The cells were subsequently disassembled in an Ar glovebox, and MST was performed on the extracted anodes. *Cell 6C-a* was a slight exception, as the graphite electrode was charged to ~7.5% state of charge (SOC) after HEXRD measurements but

before MST was performed. To account for this, a correction was applied to the dead Li measured via MST in this cell in order to directly compare HEXRD and MST measurements. As explained in ESI Section S3 †, this correction induced only an additional ~2.5% error in the dead Li in this cell compared to other cells.

2.2 Incremental Capacity Analysis

Incremental capacity (IC, or dQ/dV) analysis of the RPT cycles was used to quantify the total amount of LLI and LAM_{PE} that occurred within the tested cells via shifts or changes in the area of measured dQ/dV peaks[18,25,43]. Experimentally collected dQ/dV profiles were compared against dQ/dV profiles generated using a previously developed electrochemical model with tunable inputs for LLI and LAM_{PE}[25]. LLI and LAM_{PE} were manually tuned to minimize the root-mean-square error (RMSE) between modeled and experimental dQ/dV profiles using a Matlab-based simulation toolbox called "Alawa"[25,44]. This toolbox has been used to analyze similar pouch cells in previous work[18]. The error associated with fitting of the dQ/dV profiles to extract LLI and LAM_{PE} values was estimated to be ±5% of the fitted value, which was determined based on an analysis of the RMSE between the fitted and experimental dQ/dV profiles in the prominent peak regions (~3.45 V and ~3.6 V). The RMSE generally remained between 0.7% to 5.7% for the peak at 3.45 V and 3.3% to 14.0% for the peak at 3.6 V. LLI and LAM_{PE} values were then extracted from the curves of best fit, and representative experimental and modeled dQ/dV profiles are shown in ESI Section S4 †.

We note that not all LLI or LAM_{PE} directly contributed to capacity loss, as capacity fade is generally dictated primarily by the most dominant aging mode. We thus use the subscript "CL" to describe the amount of a given aging mode which directly contributes to capacity loss. This will be elaborated upon in Section 3.1.1. In general, we found that LLI was the dominant aging mode and closely matched the total capacity lost. Thus, we concluded that LLI was equivalent to LLI_{CL}. $LAM_{PE,CL}$, which was generally less than LAM_{PE}, accounted for the small difference between total capacity lost and LLI.

2.3 High Energy X-ray Diffraction Mapping

HEXRD is an *in situ*, quantitative method used to obtain the amount of dead Li and Li_xC_6 species in cells, as well as cathode and anode SOCs over XFC cycling[6–8,27,45–47]. By rastering a millimeter-sized X-ray beam over the entire pouch cell (~14 cm^2 cross-sectional area) in the discharged state, one can obtain both local (mm-scale) and global (electrode-scale) information about LLI from irreversibly plated Li and dead lithiated graphite[8,29,30], along with the cathode SOC[45]. The high X-ray energy, flux, and area detectors available at synchrotron sources allowed for such non-destructive analyses in a reasonable amount of time (under 3 hours). We have previously used HEXRD to quantify the amount of irreversibly plated Li, dead LiC_6, and dead LiC_{12} over the entire cell[8] and examined the spatial collocation of plated Li, dead Li_xC_6 species, and the loss of Li in the cathode in the same cells studied in this work[8]. We note the importance of care in quantification as there have been claims of amorphous Li, but for these reports the conclusions appear to be based on erroneous use of powder XRD formalisms, and these claims should be regarded with caution[48]. We here combine the HEXRD results with complementary characterization techniques which provide additional synergistic insights into degradation processes. The more dilute lithiated graphite phases, such as LiC_{18} and LiC_{30}, were only present in negligible quantities, and thus did not contribute significantly to the total amount of lithiated graphite. All HEXRD measurements were conducted in the fully discharged condition (3.0 V) of the cells. For details on the set-up of the HEXRD experiments, experimental parameters, and data analysis workflow, we refer the readers to our previous publication[30].

2.4 Mass Spectrometry Titration

After HEXRD measurements were performed, the pouch cells were disassembled in an Ar glovebox, and optical images of the graphite anodes were captured. The electrodes were then rinsed in dimethyl carbonate to remove residual electrolyte from the electrode pores. Subsequently, mass spectrometry titration (MST), which has been described in depth elsewhere[14], was used to quantify various Li-containing species present on the graphite electrodes by measuring the amount of gas evolved upon their reaction with acid. To obtain local information about SEI species and to avoid saturating the relevant ion currents on the mass spectrometer, the amount of sample titrated was limited to ~1-5 cm^2 (measured by ruler) pieces of the full graphite electrode. Although this area measurement did induce a small amount of experimental error, the errors associated with the area measurements were much less than the errors associated with baseline correction of the gas evolution signatures during MST measurements (~5-10% error)[14]. The electrode was cut using ceramic scissors to avoid corrosive reactions during the cutting process.

Three main classes of species were quantified with MST:

1. **Dead Li and dead lithiated graphite (Li_xC_6)**: This class of species encompasses both irreversibly plated Li metal and Li_xC_6 that is electronically isolated from the bulk electrode, rendering it electrochemically inactive. Li and Li_xC_6 could not be individually quantified with MST, but the cumulative amounts of Li and Li_xC_6 measured via MST and HEXRD are compared in ESI Section S5 †. This comparison reveals that MST measurements consistently yield ~20% more combined dead Li and Li_xC_6 compared to HEXRD measurements (possibly due to the presence of nanocrystalline Li deposits that are not observable in HEXRD).

2. **Solid carbonate species**: This class of species includes lithium ethylene dicarbonate (LiEDC), lithium ethylene monocarbonate (LiEMC), and Li_2CO_3. We note here that a single LiEDC is comprised of two solid carbonates, as there are two carbonate groups per LiEDC, and a single LiEDC molecule would evolve two CO_2 molecules upon acid titration. Likewise, LiEMC and Li_2CO_3 are comprised of one solid carbonate each.

3. **Lithium acetylide (Li_2C_2)**: This species likely forms as a result of the reaction of plated Li with solid carbonates in

the SEI[14,15].

Upon exposure to a 3.5 M H_2SO_4 titrant, dead Li/Li_xC_6, solid carbonates, and Li_2C_2 evolved H_2, CO_2, and C_2H_2 gas, respectively, according to Reactions 1-6. These gases were quantified with an in-line mass spectrometer (which had been previously calibrated with control solutions of each analyte gas in Ar), and the total amounts of each species were determined. Example calculations showing the conversions between the amounts of each species and the corresponding capacity losses are shown in ESI Section S4 †.

$$Li + H_2O \longrightarrow LiOH + \frac{1}{2}H_2\uparrow \quad (1)$$

$$LiC_6 + H_2O \longrightarrow LiOH + C_6 + \frac{1}{2}H_2\uparrow \quad (2)$$

$$(CH_2OCO_2Li)_2\ (\text{LiEDC}) + 2H^+ \longrightarrow (CH_2OH)_2 + 2Li^+ + 2CO_2\uparrow \quad (3)$$

$$HOCH_2CH_2OCO_2Li\ (\text{LiEMC}) + H^+ \longrightarrow (CH_2OH)_2 + Li^+ + CO_2\uparrow \quad (4)$$

$$Li_2CO_3 + 2H^+ \longrightarrow H_2O + 2Li^+ + CO_2\uparrow \quad (5)$$

$$Li_2C_2 + 2H^+ \longrightarrow 2Li^+ + C_2H_2\uparrow \quad (6)$$

2.5 Combining MST and XRD Measurements

MST and HEXRD measurements afforded complementary information which could be leveraged to gain a more holistic understanding of the degradation mechanisms that occurred within the cells. In order to combine insights about local (cm^2) degradation gained from both MST and HEXRD, we cut each electrode into multiple regions and performed MST on each region separately, as shown in ESI Section S6 †. For *Cell 6C-a*, we cut the graphite electrode strategically to isolate regions with visually similar plating features. Specifically, Regions B and C in ESI Section S6 † appeared to have a dense layer of plated Li, Region E had sparser Li plating, and Region A was largely free of Li plating. Each region was then correlated with the appropriate location on the HEXRD map of the *Cell 6C-a* anode, as shown in ESI Section S6 †. The other three cells studied were not cut along Li plating contours, and therefore similar local analyses were not performed.

It was also important to decouple the amount of Li-containing species present after formation cycling from the species formed during XFC cycling. In general, the initial SEI (containing predominantly LiF and solid carbonate species along with some Li_2C_2) is formed during formation cycling, but the SEI can evolve during fast charge cycling, especially when Li plating ensues[14]. The graphite electrode in our cells also remained ~2% lithiated after formation cycling because the 3.0 V lower cutoff potential employed during formation cycling limited the maximum graphite potential to ~1.0 V, meaning the graphite did not become fully delithiated[18]. To separate the remnant Li_xC_6 after formation cycling from the dead Li_xC_6 which formed during XFC cycling, we used a methodology which has been described in detail in previous work[8]. To determine the amount of SEI species present after formation cycling, we titrated an extracted graphite electrode from a cell (which was nominally identical to the other four cells tested before cycling) that had undergone only the formation cycling procedure to determine the "baseline" amount of each SEI species. We note that solid carbonate SEI species deposited during formation cycling are predominantly formed via the reduction of EC, and Li_2C_2 likely formed via the reduction of solid carbonate species in intimate contact with the highly reactive lithiated graphite surface[49]. We measured baseline amounts of 1.2 ± 0.1 μmol/cm^2 solid carbonates and 37 ± 7 nmol/cm^2 Li_2C_2, and we attributed any increase in solid carbonates and Li_2C_2 above the baseline amounts to additional SEI deposition during fast charge. Example calculations of XFC capacity losses due to dead Li, solid carbonates, and Li_2C_2 can be found in ESI Section S4 †. Finally, all subsequent mentions of the amounts of any Li-containing species (e.g., dead Li, solid carbonates and Li_2C_2) in this manuscript refer to the amounts generated during XFC cycling (i.e., obtained by subtracting the formation cycling baseline amounts from the total measured amounts). Since no plated Li was detected prior to XFC cycling and measurements on the graphite electrodes were conducted in the discharged state (after a slow C/20 cycle), all measured plated Li is irreversibly plated Li which formed during XFC cycling.

3 Results and Discussion

The results obtained from the combination of dQ/dV, MST, and HEXRD measurements are discussed at two length scales. At the *global* (full cell) scale, the contribution of various LLI mechanisms to the capacity fade across the cells are presented. In particular, the influence of charging rate and protocols on the nature of XFC degradation behavior is discussed. Finally, we examine two cells (*Cell 6C-a* and *Cell 6C-c*) to obtain *local* (cm^2) insights into their degradation mechanisms. We reiterate that the subscript CL is used in the proceeding section to denote LLI or LAM_{PE} which directly contributes to capacity loss, while LLI or LAM_{PE} with no subscript indicates the total amount of LLI or LAM_{PE} measured via dQ/dV.

3.1 Insights into *Global* Degradation

This sub-section discusses the *global* insights obtained from the combination of dQ/dV, HEXRD, and MST measurements.

3.1.1 Contributions of Degradation Mechanisms to Global Capacity Fade

We first sought to determine the individual contributions of the two broad categories of cell degradation —LLI and LAM_{PE} —to capacity loss in each of the four tested cells using dQ/dV analysis. LLI and LAM_{PE} can both occur simultaneously, but typically only one mode is the major contributor to capacity loss[25]. In all four of our tested cells, we determined that LLI was the major degradation mode, as LLI accounts for most —but not all —of the total

capacity lost over cycling for each of the four cells (see Figure 1(a-d)). As such, we concluded that all LLI directly contributed to capacity loss.

The remaining portion of capacity loss which was not encompassed by LLI was ~1-2% for each cell, yet LAM_{PE} was ~4-13% among the four cells, indicating that a significant portion of LAM_{PE} did not directly contribute to capacity loss (i.e., $LAM_{PE} >> LAM_{PE,CL}$). We rationalize this by assuming that LLI and LAM_{PE} may both influence capacity loss in regions of the cells with small amounts of plated Li, but LAM_{PE} is dwarfed by LLI in regions with large amounts of plated Li. Although a sizable portion of LAM_{PE} does not directly contribute to capacity loss, the accumulation of LAM_{PE} over cycling provides insights which would not otherwise be apparent from cell capacity data. For example, we find that the measured amount of LAM_{PE} for *Cells 4C-a*, *6C-a*, and *6C-b* is only ~4-7%, but it is notably higher in *Cell 6C-c* (~13%) by the end of 450 fast charge cycles, with a sudden increase in the rate of LAM_{PE} accumulation starting at ~225 cycles for *Cell 6C-c*. We will discuss further implications of this higher LAM_{PE} in *Cell 6C-c* in subsequent sections.

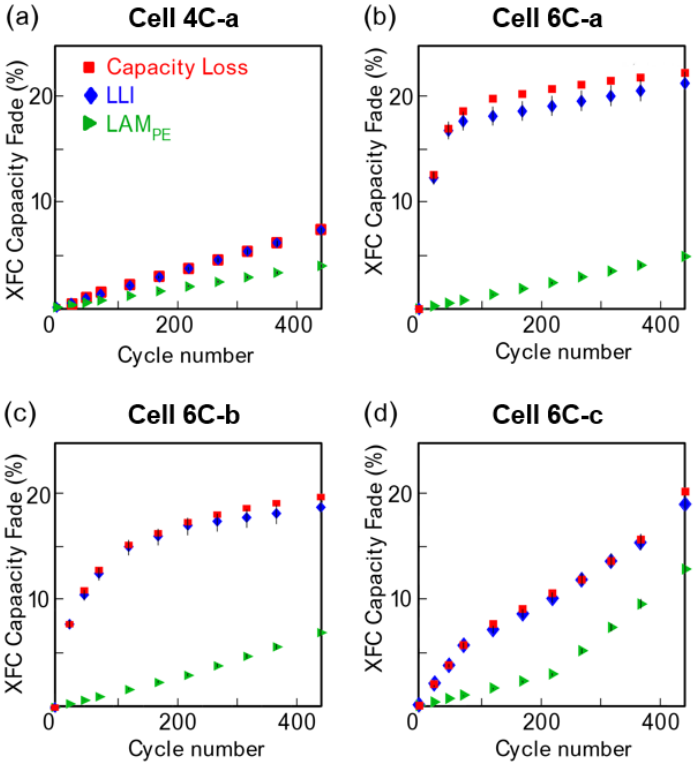

Fig. 1 Capacity loss during extreme fast charge (XFC) cycling as a function of cycle number overlaid with total LLI and LAM_{PE} obtained from dQ/dV analysis for (a) *Cell 4C-a*, (b) *Cell 6C-a*, (c) *Cell 6C-b*, (d) *Cell 6C-c*. Cycling data for these cells taken from Refs[8,29,30].

In addition to delineating between LLI and LAM_{PE}, we also quantified the contributions of specific mechanisms of LLI (plated Li, dead Li_xC_6, Li_2C_2, and solid carbonate deposition) to the amount of XFC capacity lost in each cell. We quantified each LLI mechanism individually using a combination of HEXRD and MST (as explained in Section 2.5), and any remaining lost capacity that was not accounted for by either of our employed techniques was attributed to the parasitic formation of SEI species that we could not measure using any of the techniques (e.g., LiF, oxalates, succinates, etc.)[50]. Charalambous et al. previously used HEXRD to observe the presence of LiF in SEI adjacent to plated Li deposits[6]; however, such HEXRD analyses can only be conducted *ex-situ* on anodes which have been removed from the cell casing. We expect, although cannot confirm, that the majority of the unaccounted XFC capacity loss arose from either LiF deposition on the anode, as it is typically reported to be an abundant graphite SEI component[11,12,51,52], or from other species occasionally observed from electrolyte oxidation, such as lithium oxyfluorophosphates[22].

Figure 2 shows this consolidated information across all of the cells. For the three cells cycled at 6C, dead Li and dead Li_xC_6 (measured via MST) are significant contributors to the cell capacity fade, which is consistent with previous work[8]. We note that dead Li and Li_xC_6 were also separately quantified via HEXRD. We found that the HEXRD-measured amounts of dead Li and Li_xC_6 were consistently ~20% lower than the MST-measured counterparts, possibly due to the presence of nanocrystalline Li deposits (see ESI Section S5 †). Li_2C_2 and solid carbonate species are also minor contributors to the cell capacity fade in the three cells cycled at 6C. On the other hand, *Cell 4C-a* shows almost no capacity losses from plated Li, dead Li_xC_6, solid carbonate species, or Li_2C_2. In this cell, most of the XFC capacity loss over 450 cycles (~7.5% of the pre-XFC capacity) is due to the SEI species that are unaccounted for by both HEXRD and MST. Given that the charge time per cycle in *Cell 4C-a* was 15 minutes (compared to 10 minutes for *Cells 6C-a* and *6C-b*, and *6C-c*), we hypothesize that the longer time *Cell 4C-a* spent at high voltage, as well as the absence of Li plating, resulted in an SEI that was compositionally distinct from the SEIs formed in *Cells 6C-a, b, and c*. The SEI formed during fast charging of this cell may contain LiF (which has been commonly reported as a prominent SEI component on graphite)[11,12,52] or other amorphous components. Complementary characterization (e.g., with X-ray photoelectron spectroscopy) would be needed to test this hypothesis in future work. It is also worth noting that, while almost no solid carbonate SEI species were deposited in *Cell 4C-a* during XFC, a significant amount of solid carbonate SEI species (corresponding to ~20 μmol Li) was deposited in *Cell 6C-a*. As both *Cells 4C-a* and *6C-a* were charged with CCCV protocols at different rates, we speculate that the deposition of solid carbonate SEI species is highly rate dependent, and large overpotentials are likely required to induce mossy plated Li, which ultimately reacts with electrolyte to form solid carbonate species[53,54]. CEI formation may have also contributed to LLI, especially on NMC particles near the separator, which may become more delithiated (and hence more reactive with electrolyte) compared to NMC particles close to the Al current collector.[55].

Cells 6C-a and *6C-b* had smaller amounts of capacity loss from "Other SEI" compared to *Cell 4C-a*, indicating less non-carbonate/Li_2C_2 species were deposited during XFC in these cells. *Cell 6C-c*, however, had both a large capacity loss from "Other SEI" and an anomalously high amount of LAM_{PE} (Figure 1(d)), although only a small portion of LAM_{PE} directly contributed to

capacity loss ($LAM_{PE,CL} < LAM_{PE}$). We hypothesize that heterogeneous current distributions within this cell (perhaps due to localized poor wetting in one corner of the cell, which will be discussed in Section 3.2.2) caused some regions of the cathode to become overdelithiated compared to the bulk electrode during charge. It has also been shown that NMC particles which undergo deep delithiation are prone to crack[20,56], and we observe evidence of localized NMC particle cracking in this cell as well in the partially delithiated state. The partially delithiated NMC surfaces created upon cracking would be highly reactive with the electrolyte, which can be oxidized at potentials of 4.1 V and above[17] to form soluble species in the electrolyte, such as lithium oxyfluorophosphates[17,22,23]. These soluble species may have then been reduced at the graphite electrode and deposited on the graphite surface completing a "crosstalk" mechanism in which a degradation process originating at the NMC cathode eventually results in SEI deposition at the graphite anode[12,57,58]. This speculation is consistent with our titration results (Figure 2), which show that solid carbonates and Li_2C_2 alone cannot account for the large amount of LLI in *Cell 6C-c*. Local analyses of plated Li on the anode and the SOC distribution on the cathode also support this suggestion, as will be discussed in Section 3.2.2.

Finally, we stress that the *global* capacity fade of these cells was almost completely governed by LLI, and was predominantly due to Li plating for the highest-tested 6C charge rates, which is in line with our previous work[8]. This finding has important implications for the realization of XFC charging in batteries, especially for EVs. With thicker electrodes, while the capacity of the anode increases, the propensity to irreversibly plate Li on the graphite anode also increases due to an exacerbation of the lithiation gradient across the anode thickness[59]. Thus, in order to achieve XFC charging with commercially relevant energy densities ($\geq$3mAh/cm^2 as in this work), methods will need to be developed to limit LLI through irreversible Li plating in thicker ($\geq$70 μm) electrodes. Thus, cell improvements to enable XFC cycling in commercially relevant cells should generally focus more on ways to minimize Li plating, such as enhanced electrolyte wetting, greater ionic conductivity in the electrolyte, or improved anode architectures[60,61].

3.1.2 *Global* Correlations Between Degradation Products

Having now established that Li plating plays a significant role in XFC capacity fade at a charging rate of 6C, we turn to ways in which Li plating can in turn induce other LLI mechanisms. For example, plated Li can block deintercalation pathways for Li_xC_6[29], or it can react with SEI or electrolyte components to form Li-containing salts, which depletes the Li inventory in the cell[9]. Thus, plotting the *global* amounts of various LLI products in Figure 2 as a function of the total plated Li can shed light on how additional LLI mechanisms are correlated to Li plating during XFC cycling. Figure 3 shows the *global* correlations between the amounts of various SEI species and the total amount of irreversibly plated Li (measured via HEXRD) over the four cells analyzed in this study. We note that the plotted amounts of Li_2C_2, solid carbonates and Li_xC_6 in Figure 3 represent the amounts formed only during XFC cycling since the baseline amounts present after formation cycling have been subtracted out.

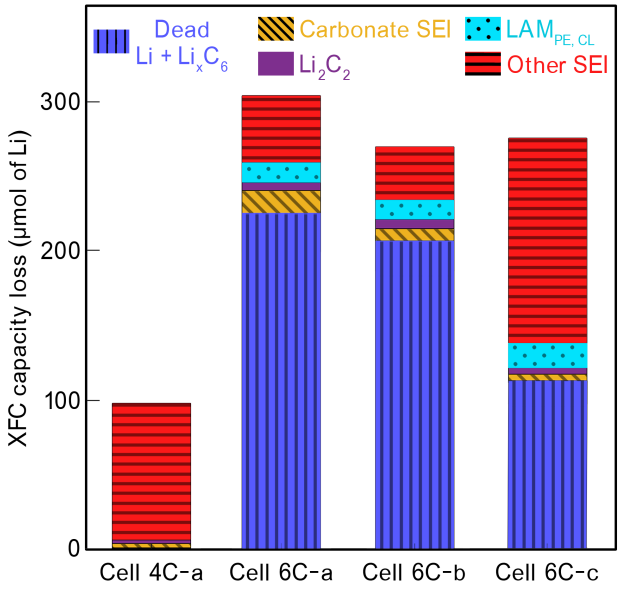

Fig. 2 Contributions of various degradation mechanisms — including combined dead plated Li and dead Li_xC_6 formation (measured via MST), solid carbonate SEI deposition (measured via MST), Li_2C_2 formation (measured via MST), loss of positive electrode active material ($LAM_{PE,CL}$, measured via dQ/dV), and other SEI deposition (not captured by any of the applied characterization techniques) — to the XFC capacity loss of four tested cells after 450 XFC cycles. Plated Li and dead Li_xC_6 have also been quantified for these cells via HEXRD in previous publications[8,30].

In Figure 3(a), we find that the amount of Li_2C_2 SEI species is positively correlated with the amount of plated Li across the four cells. The Li_2C_2 observed in *Cell 4C-a* likely formed via the reduction of solid carbonate species in contact with the lithiated graphite surface over many cycles, as no plated Li was measured in this cell. The increase in Li_2C_2 above the amount observed in *Cell 4C-a* for *Cells 6C-a*, *6C-b*, and *6C-c*, which all had plated Li, is therefore attributed to the reaction of the outer surface of plated Li deposits with other SEI components[14,15]. This hypothesis implicitly assumes that dead plated Li is intertwined with other SEI species on the anode, such that Li and other SEI species may be in intimate contact. We speculate that, as more dead Li is deposited, the contact area between dead Li and solid carbonate SEI species increases, resulting in additional conversion of solid carbonates to Li_2C_2.

The amount of solid carbonate SEI species is also positively correlated with the amount of plated Li, as shown in Figure 3(b). We hypothesize that solid carbonate deposition during XFC cycling occurs via a reaction of plated Li with electrolyte, and is thus governed by the amount of plated Li surface area in contact with electrolyte. The correlation between plated Li and solid carbonates may be superlinear (rather than linear), but we acknowledge that this is heavily influenced by *Cell 6C-a*, which had a substantially larger amount of solid carbonates than would be expected based on a linear trend with the other three cells, so more

data points would be needed to further validate this trend. Previous studies have reported a similar superlinear correlation between the amount of solid carbonates deposited and the amount of fast charge cycles completed, which the authors attributed to a Li "breakthrough" effect, whereby Li deposited after extended cycling became mossy and protruded out of the existing SEI, resulting in a sudden increase in solid carbonate deposition due to intimate contact between the mossy Li and the electrolyte solvent[14].

Finally, we observe a near-linear relationship between the amount of dead Li_xC_6 and irreversibly plated Li across the cells in Figure 3(c). Our previous work has shown that dead Li and Li_xC_6 in these cells are not only correlated at the cell-scale, but also collocated at the local scale[8]. Such collocation may arise due to lithiated graphite particle dislodgement during rapid lithiation, which can be further exacerbated by interparticle stresses induced by plated Li[6,7]. Plated Li may also physically block pathways for Li^+ transport through the graphite SEI, which could prevent lithiated graphite from being delithiated, as discussed in our earlier work[29]. We refer readers to ESI Section S7 † for more information about how these *global* correlations between plated Li and other species hold over the local scale in specific regions of *Cell 6C-a*.

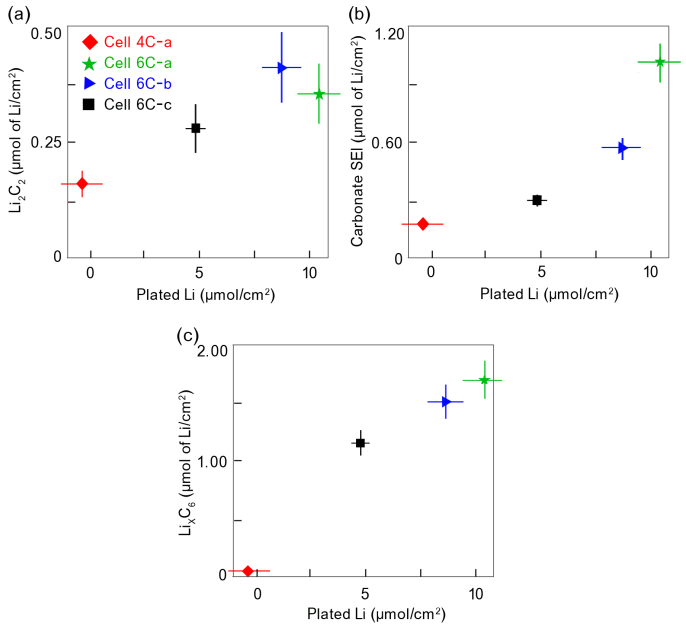

Fig. 3 *Global* correlations between the amounts of (a) Li_2C_2 (measured via MST), (b) solid carbonate SEI species (measured via MST), and (c) lithiated graphite (measured via HEXRD) formed during XFC and the amount of irreversibly plated Li (measured via HEXRD) across four different cells. The presented data are *global* measurements normalized over the entire cell area (~14.9 cm^2). The total amount of plated Li and LiC_6 measured via HEXRD in each of these cells has also been reported in previous publications[8,30].

3.2 Quantification of *Local* Degradation Mechanisms

This section discusses the *local* insights into cell degradation, as obtained from the combination of dQ/dV, HEXRD, and MST. "Local" here refers to ~1-5 cm^2 regions of the full graphite electrode, which surprisingly show degradation behavior that deviates from the *global* full electrode average degradation behavior. In particular, we discuss the variation of degradation mechanisms across the full area of *Cell 6C-a* and the anomalously high LAM_{PE} observed in *Cell 6C-c*. *Cell 6C-a* was chosen for local analysis because it was strategically cut along the boundaries of regions with distinct Li plating patterns, whereas the other cells were cut in a grid-like manner which did not necessarily isolate regions with homogeneous coverage of plated Li. *Cell 6C-c* was also chosen for local analysis because one particular region exhibited anomalously low cathode SOC which was collocated with an unidentified SEI species on the adjacent area of the anode. We speculate that this unidentified SEI species, which diffracts in the region of plated Li, may be a thick film of lithium oxyfluorophosphates that is deposited due to local electrolyte degradation spurred by the reactive, partially delithiated cathode.

3.2.1 *Cell 6C-a*: Heterogeneity of LLI Mechanisms Across the Cell

The graphite electrode extracted from *Cell 6C-a* was cut into six regions (labeled A-F in Figure 4(a)) which had visibly distinct Li plating patterns, and each region was separately titrated using MST. Region A (the outer edge region indicated by the dashed box in Figure 4(a)) had no visible plated Li and likely remained at lower lithiation states (based on the limited amount of SEI species and Li_xC_6 measured via MST) during cycling compared to Regions B-F. We note that the graphite electrode was oversized compared to the cathode by ~0.8 cm^2, so Li^+ preferentially inserted into the central regions of the graphite electrode during XFC. However, Region A (where no plated Li is visible) encompasses ~6.6 cm^2 of electrode area, which is much larger than the ~0.8 cm^2 anode overhang region. This reveals the important role of edge effects in cells with anode overhang. Even though only ~0.8 cm^2 of the graphite electrode area was not directly covered by the cathode, the amount of plated Li was substantially reduced even in the the edge region of the graphite which was covered by the cathode. This may have occurred due to poor electrolyte wetting at the edges of the cathode, which rendered the edge regions of the adjacent graphite less utilized. Another possible explanation is that Li^+ ions liberated from the NMC cathode edges during fast charge had ample available graphite sites within close proximity, allowing Li^+ to be inserted over a broad area along the edge region. This in turn reduced the graphite SOC on the edges compared to the center and decreased the propensity for Li plating in the edge region —even in some edge regions which were covered by the cathode.

There was also a distribution of Li plating patterns in the central regions. Region E, for example, appeared to have a sparse amount of plated Li, while Regions B and C had optically apparent dense layers of plated Li. As discussed in Section 2.5, each electrode piece was correlated to the appropriate location on the HEXRD map of *Cell 6C-a*, allowing us to compare MST and HEXRD measurements over specific regions of the electrode. With a broad distribution of plated Li coverage (measured in μmol Li/cm^2) among the different regions, we could uncover relation-

ships between local plated Li coverage and the local amounts of SEI and Li_xC_6 in each region. The combined results of this analysis are shown in Figure 4.

Several interesting trends are apparent from this *local* (~1-5 cm^2) analysis. First, as shown in Figure 4(b), the amount of solid carbonate species locally is weakly correlated with the amount of plated Li, although there is significantly more scatter in the data compared to the *global* correlation in Figure 3(b). Solid carbonate species deposited during fast charge have been previously proposed to form via the reaction of plated Li with the electrolyte solvent[14]. Thus, if the plated Li is columnar or otherwise uniform in morphology, it is likely to remain well-encapsulated by the existing SEI, and minimal additional solid carbonates would be deposited during charge. On the other hand, mossy Li, which is commonly observed during fast charging[53,62], has a high exposed surface area and is more prone to react with electrolyte to produce additional solid carbonate species. We thus speculate that the morphology of plated Li may vary substantially across the different regions of the electrode, with regions covered by mossy Li containing large amounts of solid carbonate species. Figure 4(c) shows a yet weaker correlation between the amount of Li_2C_2 deposited during fast charge and the amount of plated Li, despite the stronger linear correlation at the *global* scale. Although there is considerable scatter in the data, as Li_2C_2 has been proposed to form via the reaction of plated Li with solid carbonates in the SEI[14,15], this finding may suggest that the surface area of plated Li in intimate contact with carbonate SEI species varies across the cell. We speculate that an uneven stack pressure distribution on this cell may have induced this behavior[63]. Regions B and D on the left side of the cell (as viewed from the perspective of Figure 4(a)) had relatively more Li_2C_2 —possibly due to the compression of the cell which promoted contact between plated Li and Li_2C_2 —while Regions C and F on the right side of the cell had relatively less Li_2C_2 (perhaps similarly due to less local applied pressure). Finally, the dead Li_xC_6 (measured via HEXRD) shows a linear correlation (with far less scatter compared to the other species) with the amount of plated Li in each region of the cell (Figure 4(d)), which is similar to that observed at the *global* scale and is consistent with previous work[8]. The data shown in Figure 4 is plotted onto Figure 3 in ESI Section S7 † to provide further insight into how each correlation holds over a broad range of plated Li coverage from the *global* to *local* scale.

In general, *local* correlations between the amount of plated Li and SEI species/Li_xC_6 (analyzed on ~1-5 cm^2 pieces of a full electrode) appear weaker than those observed at the *global* scale. This demonstrates the important role of heterogeneities (such as the morphology of plated Li deposits, stack pressure distribution, and electrode wetting uniformity) that arise within a cell during XFC cycling. We note that these heterogeneities are not unique to our study, as similar heterogeneous Li plating patterns have been observed in other pouch cells that underwent XFC cycling[18,28]. Going forward, it will be important to better understand the origin of these heterogeneities using additional characterization techniques (e.g., scanning electron microscopy of Li deposits, external pressure sensors, etc.) so that future improvements to the anode, electrolyte, and cell design can be tailored to minimize Li plating.

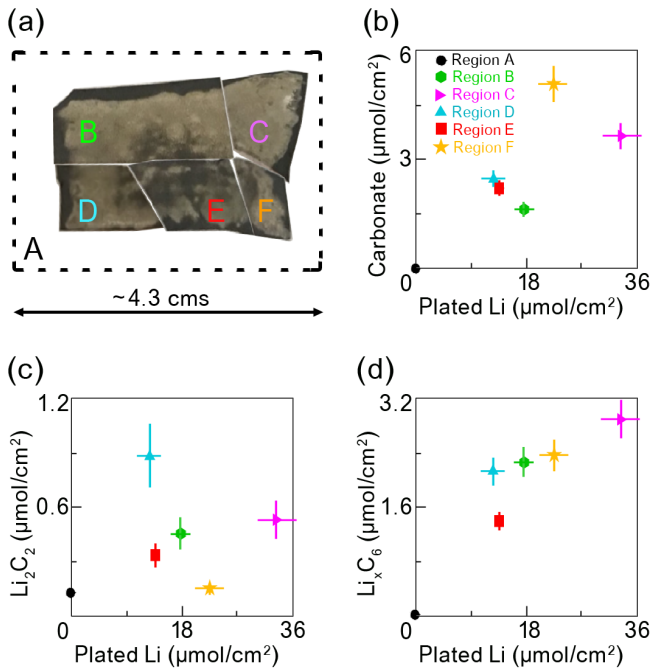

Fig. 4 Local variation of degradation mechanisms in *Cell 6C-a*. (a) Image of electrode that was cut into six regions (marked A-F). Each region was separately titrated to quantify Li and SEI species. Correlation between the amount of plated Li (measured via HEXRD) and (b) carbonate SEI (measured via MST); (c) Li_2C_2 (measured via MST); and (d) dead Li_xC_6 (measured via HEXRD) formed during XFC cycling per unit area of anode measured across the six regions. The total amount of plated Li and LiC_6 measured via HEXRD in this cell have also been reported in previous publications[8,30].

3.2.2 *Cell 6C-c*: Influence of *Local* LAM_{PE} on LLI and XFC Capacity Fade

Cell 6C-c exhibits anomalous behavior compared to the other cells charged at 6C in many ways. Although the XFC capacity loss (~20%) is about the same as *Cells 6C-a* and *6C-b* by the end of cycling, the measured amount of irreversibly plated Li is significantly lower in *Cell 6C-c* (shown in Figure 2), and a significantly higher portion of LLI is unaccounted for by HEXRD or MST. We also see that the trend in the XFC capacity fade over cycling for *Cell 6C-c* is very different from *Cells 6C-a* and *6C-b* (Figure 1(b-d)). While the capacity fade for *Cells 6C-a* and *6C-b* plateaus beyond 200 XFC cycles, the capacity fade for *Cell 6C-c* continues to increase after 200 cycles, which suggests a different degradation mechanism may have occurred. Additionally, while the LAM_{PE} of *Cells 6C-a* and *6C-b* is fairly linear with cycle number, the LAM_{PE} of *Cell 6C-c* increases abruptly around 200 cycles. In Figure 5(a), we emphasize these changes by taking the derivative of the total XFC capacity fade, LLI, and LAM_{PE} with respect to cycle number so we can better visualize how degradation modes evolve in *Cell 6C-c* over cycling[39]. $d(LAM_{PE})/dN$ is constant up to ~200 cycles, followed by an abrupt quadrupling of the rate at cycle ~225 and then another constant rate regime for the remaining ~200 cycles.

The optical image of the anode (Figure 5(b)) after XFC cycling along with the HEXRD maps in Figure 5(c-d) provide further in-

sight into the possible origin and consequences of this sudden spike in LAM_{PE}. We focus on the bottom right corner, which is highlighted by the cyan box in Figure 5(b-d). In the boxed region, integration of the HEXRD peak related to plated Li suggests an anomalously large amount of plated Li in the region (Figure 5(c)). However, there is no obvious optical evidence of plated Li in this region (Figure 5(b)), and the HEXRD map of LiC_6 (see ESI Section S8 †), which is typically collocated with plated Li, does not show any notable features in this region[6,8]. These observations led us to conclude in a previous work that the bottom right corner likely did not contain plated Li[30]. Here, MST measurements of the amount of dead Li also suggest that the bottom right corner does not contain plated Li. In fact, the combined amount of dead Li and dead Li_xC_6 in this region is within error of the amount of Li_xC_6 present after formation cycling (~2 μmol/cm^2 dead Li).

A closer look at Figure 5(d) also shows a local decrease in the Li occupancy (per unit cell of NMC) in the cyan box, calculated from the NMC unit cell volume. A smaller NMC unit cell volume is reflective of a smaller amount of Li per unit cell of NMC[64], since a lower amount of Li close to the discharged state of the cell results in a contraction of the unit cell along its *c* axis[65]. Thus, the cathode in the cyan box region is less lithiated than the majority of the electrode, suggesting that LLI occurs in this region from an unknown source[8].

We hypothesize that the cyan box region consists of a large cluster of cracked NMC particles, which are at ~20% lower lithiation state than the majority of the electrode due to particle cracking that occurred suddenly at cycle ~225 during fast charge. This notion is supported by previous studies, which revealed that loss of cathode active material can occur along the edges of the electrode and suggests that particle damage or particle delamination may occur on the electrode edges during the cutting process[56]. Additionally, the separator completely encased the cathode in our study, and the creased separator in the corner region of *Cell 6C-c* may have imparted additional stress on the cathode particles or influenced the wetting of the electrode pores, which may have resulted in particle cracking[66,67]. This underscores the important role of edge effects, which should be closely analyzed in future studies of pouch cells with wrapped separators. Mn dissolution could also play a role in the lower lithiation states of the NMC particles in the cyan box region, but a recent study of graphite/NMC pouch cells which underwent similar cycling procedures revealed that less than 0.1% of the Mn from NMC dissolved into the electrolyte and deposited on the anode[40].

It is also notable that the other cathode regions with lower lithiation states (e.g., the middle-left portion of Figure 5(d)) correspond to regions of high Li plating, which may be deposited predominantly during the first ~150 XFC cycles (corresponding to the high early values of d(LLI)/dN) in Figure 5(a)), as the same collocation of delithiated NMC and plated Li is also observed in *Cells 6C-a* and *6C-b*. As previously noted, however, MST measurements suggest that the amount of plated Li is minimal in the cyan box region of the *Cell 6C-c* graphite anode despite the large intensity of a HEXRD peak that overlaps with Li in this region. We thus speculate that some unknown species which diffracts at a similar Bragg angle to Li is deposited on the anode due to a crosstalk mechanism, whereby the oxidized electrolyte species formed at the cracked NMC cathode particle surfaces migrate to the graphite anode and ultimately deposit the graphite surface. Based on previous literature, the onset for electrolyte oxidation may occur on NMC surfaces at as low as 4.1-4.2 V[17]. Thus, it is possible that the delithiated NMC in the cyan box region was reactive towards the electrolyte. Whereas most of the NMC particles only reach ~4.1 V intermittently during XFC charging protocol, cracked particles may have poor electronic connectivity to the bulk electrode, and thus remained at a high oxidative potential for the entirety of cycling, reacting constantly with the electrolyte over time. The species formed on the graphite anode could be a lithium oxyfluorophosphate species, which has been proposed to form due to electrolyte oxidation on NMC[22]. These species do not have well-studied scattering behavior and may overlap with the Li HEXRD peak, as we observe in Figure 5(c). We acknowledge, however, that this scattering behavior could arise from a different unidentified species, and we encourage those who conduct similar scattering experiments in the future to attempt to identify the true origin. More commonly reported SEI species, such as LiF, do not have HEXRD peaks which overlap with Li and are therefore unlikely to explain the observed behavior[6]. With all this in mind, we propose that local NMC particle cracking in the cyan box region occurred after ~225 cycles due to fatigue induced by separator creasing effects, resulting in the sudden spike in LAM_{PE} shown in Figure 5(a)). This cracking then resulted in a crosstalk mechanism, whereby oxidized electrolyte species formed at the cracked NMC were ultimately reduced on the graphite surface. We thus observed an increase in d(LLI)/dN after ~225 cycles (shown in Figure 5(a)) and detected an unknown species on the graphite surface with a HEXRD peak which overlaps with Li (shown in Figure 5(c)).

In all, through a combination of different analytical and experimental techniques, we provide some evidence for local crosstalk between the electrodes. Additionally, although LLI dominates capacity fade in the cells *globally*, the *local* mechanism of degradation is likely more variable, and LAM_{PE} can play a non-trivial role. Such an analysis would not be possible if the characterization techniques employed in this work were used individually.

4 Conclusions

In this work, we elucidated and quantified specific degradation mechanisms — both locally and across full electrodes — in LIBs that underwent 450 XFC (4C-6C charging rates) cycles. This degradation analysis was done multimodally, using *global* electrochemical analyses (dQ/dV) complemented by *local* HEXRD and MST measurements. We found that LLI primarily governs the capacity fade of the four tested cells, predominantly through additional SEI formation at a charging rate of 4C and through irreversible Li plating on the anode at 6C. In the cells cycled at 6C, LLI mechanisms such as dead lithiated graphite and SEI formation accounted for ~20% of the observed capacity fade, and correlations revealed between each species uncovered physical insights into the nature of each degradation mechanism. While we found evidence for the existence of LAM_{PE} in all cells, the amount of

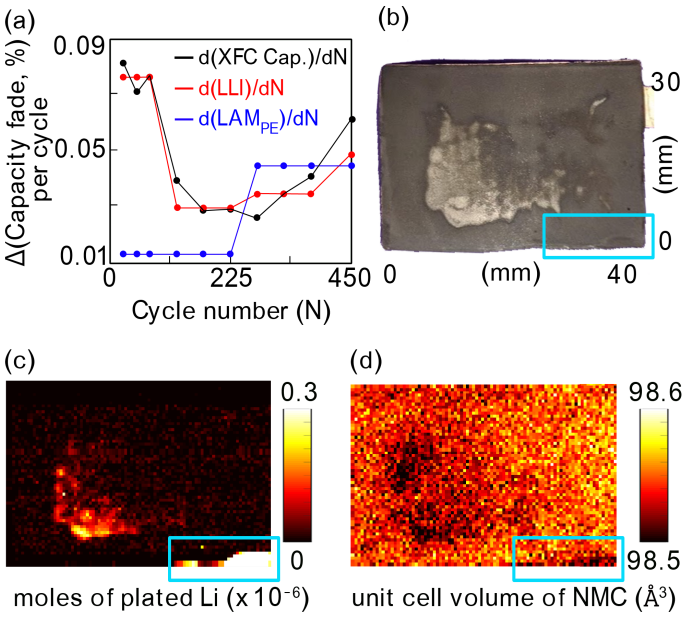

Fig. 5 Indirect influence of the *local* LAM_{PE} (bottom right corner, highlighted by the cyan box) on LLI and XFC capacity loss in *Cell 6C-c*. (a) Evolution of the rate of LLI, LAM_{PE} and cell capacity fade accumulation over XFC cycling, as calculated from Figure 1d. Each data point was calculated using the expression (Cap(i+1)–Cap(i))/(N(i+1)–N(i)), where Cap refers to XFC Cap., LLI, or LAM_{PE}, i refers to a data point index, and N refers to the cycle number. (b) An optical image of the extracted anode after 450 XFC cycles, showing regions with optically apparent irreversibly plated Li. Cyan box region shows no visually apparent plated Li. (c) HEXRD map of irreversibly plated Li on the anode in the discharged condition after 450 XFC cycles. Region of high "plated Li" XRD peak intensity in cyan box likely does not arise from plated Li, as no visual evidence of plated Li is observed in panel b. (d) HEXRD map of the NMC unit cell volume (which is correlated with the average Li per unit cell), showing relatively higher delithiation in cyan box region compared to majority of electrode area.

LAM_{PE} was dwarfed by the amount of LLI due to SEI formation at 4C rates and due to Li plating at 6C rates. Local LAM_{PE} did, however, play an important role in one cell, where physical degradation of one region of the cathode likely spurred a chain of events that ultimately resulted in additional SEI deposition on the anode. The depth of insights gleaned in this work were made possible by the synergy of complementary characterization techniques employed, and we recommend a similar multimodal approach be utilized in future studies of degradation during XFC cycling.

Author Contributions

EJM conducted the MST experiments and associated data analysis under BDM's guidance. PPP, CC, and VT conducted the HEXRD experiments and analysis, while HGS, MFT and JNW helped with the HEXRD data analysis. TRT and EJD conducted the IC analysis and XFC cycling of the cells. SET, ARD, and ANJ assembled the cells and conducted formation cycling on them. EJM and PPP combined the MST, HEXRD, and IC analyses and wrote the manuscript.

Conflicts of interest

There are no conflicts to declare.

Acknowledgements

Funding was provided from the Vehicle Technologies Office of the U.S. Department of Energy's Office of Energy Efficiency and Renewable Energy under the guidance of the Advanced Battery Cell Research Program (eXtreme fast charge Cell Evaluation of Lithium-ion batteries, XCEL). E.J.M acknowledges support from the National Science Foundation Graduate Research Fellowship Program under Grant DGE 1106400. Stanford Synchrotron Radiation Lightsource, SLAC National Accelerator Laboratory, is supported by the U.S. Department of Energy, Office of Science, Office of Basic Energy Sciences under Contract No. DE-AC02-76SF00515. Testing and cycling of the cells were carried out under the Battelle Energy Alliance, LLC under Contract No. DE-AC07-05ID14517 for Idaho National Laboratory with the U.S. Department of Energy. The XRD experiments were conducted at the beamline 11-ID-B at the Advanced Photon Source, operated by Argonne National Laboratory and at beamline 28-ID-2 at National Synchrotron Light Source II, operated by Brookhaven National Laboratory under Contract No. DE-SC0012704. Drs. Olaf Borkiewicz, Uta Ruett and Jiaming Bai helped set up the XRD experiments at APS and NSLS-II. Part of the HEXRD data post-processing was carried out using computational resources from Extreme Science and Engineering Discovery Environment (XSEDE), funded by the National Science Foundation under contract ACI-1053575.

Notes and references

1 *World Energy Outlook*, 2020, https://www.iea.org/reports/world-energy-outlook-2020.

2 T. Gersdorf, R. Hensley, P. Hertzke, P. Schaufuss and A. Tschiesner, *The road ahead for e-mobility*, 2021, https://www.mckinsey.com/industries/automotive-and-assembly/our-insights/the-road-ahead-for-e-mobility.

3 S. Ahmed, I. Bloom, A. N. Jansen, T. Tanim, E. J. Dufek, A. Pesaran, A. Burnham, R. B. Carlson, F. Dias, K. Hardy *et al.*, *Journal of Power Sources*, 2017, **367**, 250–262.

4 A. Tomaszewska, Z. Chu, X. Feng, S. O'Kane, X. Liu, J. Chen, C. Ji, E. Endler, R. Li, L. Liu *et al.*, *ETransportation*, 2019, **1**, 100011.

5 T. Waldmann, B.-I. Hogg and M. Wohlfahrt-Mehrens, *Journal of Power Sources*, 2018, **384**, 107–124.

6 H. Charalambous, O. J. Borkiewicz, A. M. Colclasure, Z. Yang, A. R. Dunlop, S. E. Trask, A. N. Jansen, I. D. Bloom, U. Ruett, K. M. Wiaderek *et al.*, *ACS Energy Letters*, 2021, **6**, 3725–3733.

7 D. P. Finegan, A. Quinn, D. S. Wragg, A. M. Colclasure, X. Lu, C. Tan, T. M. Heenan, R. Jervis, D. J. Brett, S. Das *et al.*, *Energy & Environmental Science*, 2020, **13**, 2570–2584.

8 P. P. Paul, V. Thampy, C. Cao, H.-G. Steinrück, T. R. Tanim, A. R. Dunlop, E. J. Dufek, S. E. Trask, A. N. Jansen, M. F.

Toney, Weker and J. Nelson, *Energy & Environmental Science*, 2021, **14**, 4979–4988.

9 N. R. Geise, R. M. Kasse, J. Nelson Weker, H.-G. Steinrück and M. F. Toney, *Chemistry of Materials*, 2021, **33**, 7537–7545.

10 L. Wang, A. Menakath, F. Han, Y. Wang, P. Y. Zavalij, K. J. Gaskell, O. Borodin, D. Iuga, S. P. Brown, C. Wang *et al.*, *Nature chemistry*, 2019, **11**, 789–796.

11 C. Cao, I. I. Abate, E. Sivonxay, B. Shyam, C. Jia, B. Moritz, T. P. Devereaux, K. A. Persson, H.-G. Steinrück and M. F. Toney, *Joule*, 2019, **3**, 762–781.

12 D. Strmcnik, I. E. Castelli, J. G. Connell, D. Haering, M. Zorko, P. Martins, P. P. Lopes, B. Genorio, T. Østergaard, H. A. Gasteiger *et al.*, *Nature Catalysis*, 2018, **1**, 255–262.

13 E. J. McShane, H. K. Bergstrom, P. J. Weddle, D. E. Brown, A. M. Colclasure and B. D. McCloskey, *ACS Energy Letters*, 2022, **7**, 2734–2744.

14 E. J. McShane, A. M. Colclasure, D. E. Brown, Z. M. Konz, K. Smith and B. D. McCloskey, *ACS Energy Letters*, 2020, **5**, 2045–2051.

15 M.-T. Fonseca Rodrigues, V. A. Maroni, D. J. Gosztola, K. P. Yao, K. Kalaga, I. A. Shkrob and D. P. Abraham, *ACS Applied Energy Materials*, 2018, **2**, 873–881.

16 J. Shim, R. Kostecki, T. Richardson, X. Song and K. A. Striebel, *Journal of power sources*, 2002, **112**, 222–230.

17 S. E. Renfrew and B. D. McCloskey, *ACS Applied Energy Materials*, 2019, **2**, 3762–3772.

18 T. R. Tanim, E. J. Dufek, M. Evans, C. Dickerson, A. N. Jansen, B. J. Polzin, A. R. Dunlop, S. E. Trask, R. Jackman, I. Bloom *et al.*, *Journal of The Electrochemical Society*, 2019, **166**, A1926.

19 T. R. Tanim, Z. Yang, A. M. Colclasure, P. R. Chinnam, P. Gasper, Y. Lin, L. Yu, P. J. Weddle, J. Wen, E. J. Dufek *et al.*, *Energy Storage Materials*, 2021, **41**, 656–666.

20 T. R. Tanim, Z. Yang, D. P. Finegan, P. R. Chinnam, Y. Lin, P. J. Weddle, I. Bloom, A. M. Colclasure, E. J. Dufek, J. Wen *et al.*, *Advanced Energy Materials*, 2022, **12**, 2103712.

21 J. Christensen and J. Newman, *Journal of the Electrochemical Society*, 2005, **152**, A818.

22 Y. Yu, P. Karayaylali, Y. Katayama, L. Giordano, M. Gauthier, F. Maglia, R. Jung, I. Lund and Y. Shao-Horn, *The Journal of Physical Chemistry C*, 2018, **122**, 27368–27382.

23 T. M. Østergaard, L. Giordano, I. E. Castelli, F. Maglia, B. K. Antonopoulos, Y. Shao-Horn and J. Rossmeisl, *The Journal of Physical Chemistry C*, 2018, **122**, 10442–10449.

24 C. Cao, T. P. Pollard, O. Borodin, J. E. Mars, Y. Tsao, M. R. Lukatskaya, R. M. Kasse, M. A. Schroeder, K. Xu, M. F. Toney *et al.*, *Chemistry of Materials*, 2021, **33**, 7315–7336.

25 M. Dubarry, C. Truchot and B. Y. Liaw, *Journal of power sources*, 2012, **219**, 204–216.

26 I. Bloom, A. N. Jansen, D. P. Abraham, J. Knuth, S. A. Jones, V. S. Battaglia and G. L. Henriksen, *Journal of Power Sources*, 2005, **139**, 295–303.

27 K. P. Yao, J. S. Okasinski, K. Kalaga, I. A. Shkrob and D. P. Abraham, *Energy & Environmental Science*, 2019, **12**, 656–665.

28 H. Charalambous, D. P. Abraham, A. R. Dunlop, S. E. Trask, A. N. Jansen, T. R. Tanim, P. R. Chinnam, A. M. Colclasure, W. Xu, A. A. Yakovenko *et al.*, *Journal of Power Sources*, 2021, **507**, 230253.

29 T. R. Tanim, P. P. Paul, V. Thampy, C. Cao, H.-G. Steinrück, J. N. Weker, M. F. Toney, E. J. Dufek, M. C. Evans, A. N. Jansen *et al.*, *Cell Reports Physical Science*, 2020, **1**, 100114.

30 P. P. Paul, C. Cao, V. Thampy, H.-G. Steinrück, T. R. Tanim, A. R. Dunlop, E. J. Dufek, S. E. Trask, A. N. Jansen, J. N. Weker and M. F. Toney, *ACS Applied Energy Materials*, 2021.

31 C. Uhlmann, J. Illig, M. Ender, R. Schuster and E. Ivers-Tiffée, *Journal of Power Sources*, 2015, **279**, 428–438.

32 Z. M. Konz, E. J. McShane and B. D. McCloskey, *ACS Energy Letters*, 2020, **5**, 1750–1757.

33 D. E. Brown, E. J. McShane, Z. M. Konz, K. B. Knudsen and B. D. McCloskey, *Cell Reports Physical Science*, 2021, **2**, 100589.

34 M. Petzl and M. A. Danzer, *Journal of Power Sources*, 2014, **254**, 80–87.

35 D. Anseán, M. Dubarry, A. Devie, B. Liaw, V. García, J. Viera and M. González, *Journal of Power Sources*, 2017, **356**, 36–46.

36 T. Waldmann and M. Wohlfahrt-Mehrens, *Electrochimica Acta*, 2017, **230**, 454–460.

37 T. Waldmann, J. B. Quinn, K. Richter, M. Kasper, A. Tost, A. Klein and M. Wohlfahrt-Mehrens, *Journal of The Electrochemical Society*, 2017, **164**, A3154.

38 P. R. Chinnam, T. R. Tanim, E. J. Dufek, C. C. Dickerson and M. Li, *Journal of Energy Storage*, 2022, **46**, 103782.

39 B.-R. Chen, M. R. Kunz, T. R. Tanim and E. J. Dufek, *Cell Reports Physical Science*, 2021, **2**, 100352.

40 T. R. Tanim, Z. Yang, D. P. Finegan, P. R. Chinnam, Y. Lin, P. J. Weddle, I. Bloom, A. M. Colclasure, E. J. Dufek, J. Wen *et al.*, *Advanced Energy Materials*, 2022, 2103712.

41 P. P. Paul, E. J. McShane, A. M. Colclasure, N. Balsara, D. E. Brown, C. Cao, B.-R. Chen, P. R. Chinnam, Y. Cui, E. J. Dufek *et al.*, *Advanced Energy Materials*, 2021, **11**, 2100372.

42 P. R. Chinnam, A. M. Colclasure, B.-R. Chen, T. R. Tanim, E. J. Dufek, K. Smith, M. C. Evans, A. R. Dunlop, S. E. Trask, B. J. Polzin *et al.*, *ACS Applied Energy Materials*, 2021.

43 C. R. Birkl, M. R. Roberts, E. McTurk, P. G. Bruce and D. A. Howey, *Journal of Power Sources*, 2017, **341**, 373–386.

44 T. R. Tanim, M. G. Shirk, R. L. Bewley, E. J. Dufek and B. Y. Liaw, *Journal of Power Sources*, 2018, **381**, 56–65.

45 G. S. Mattei, Z. Li, A. A. Corrao, C. Niu, Y. Zhang, B. Liaw, C. C. Dickerson, J. Xiao, E. J. Dufek and P. G. Khalifah, *Chemistry of Materials*, 2021, **33**, 2378–2386.

46 L. Su, H. Charalambous, Z. Cui and A. Manthiram, *Energy & Environmental Science*, 2022, **15**, 843–854.

47 Z. Yang, H. Charalambous, Y. Lin, S. E. Trask, L. Yu, J. Wen, A. Jansen, Y. Tsai, K. M. Wiaderek, Y. Ren *et al.*, *Journal of Power Sources*, 2022, **521**, 230961.

48 L. Su, H. Charalambous, Z. Cui and A. Manthiram, *Energy & Environmental Science*, 2022, **15**, 843–854.

49 G. V. Zhuang, K. Xu, H. Yang, T. R. Jow and P. N. Ross, *The Journal of Physical Chemistry B*, 2005, **109**, 17567–17573.

50 L. Zhao, I. Watanabe, T. Doi, S. Okada and J.-i. Yamaki, *Journal of power sources*, 2006, **161**, 1275–1280.

51 S.-B. Son, D. Robertson, Z. Yang, Y. Tsai, S. Lopykinski and I. Bloom, *Journal of The Electrochemical Society*, 2020, **167**, 140506.

52 M. Nie, D. Chalasani, D. P. Abraham, Y. Chen, A. Bose and B. L. Lucht, *The Journal of Physical Chemistry C*, 2013, **117**, 1257–1267.

53 Y. Wang, D. Dang, X. Xiao and Y.-T. Cheng, *Energy Storage Materials*, 2020, **26**, 276–282.

54 A. S. Ho, D. Y. Parkinson, D. P. Finegan, S. E. Trask, A. N. Jansen, W. Tong and N. P. Balsara, *ACS nano*, 2021, **15**, 10480–10487.

55 Y. Yang, R. Xu, K. Zhang, S.-J. Lee, L. Mu, P. Liu, C. K. Waters, S. Spence, Z. Xu, C. Wei *et al.*, *Advanced Energy Materials*, 2019, **9**, 1900674.

56 G. Zan, J. Zhang, F. Monaco, S. Gul, G. Qian, J. Li, D. J. Vine, P. Cloetens, W. Yun, P. Pianetta *et al.*, *Journal of Materials Chemistry A*, 2021.

57 B. Michalak, B. B. Berkes, H. Sommer, T. Brezesinski and J. Janek, *The Journal of Physical Chemistry C*, 2017, **121**, 211–216.

58 R. Sahore, F. Dogan and I. D. Bloom, *Chemistry of Materials*, 2019, **31**, 2884–2891.

59 Y. Liu, Y. Zhu and Y. Cui, *Nature Energy*, 2019, **4**, 540–550.

60 N. Gao, S. Kim, P. Chinnam, E. J. Dufek, A. M. Colclasure, A. Jansen, S.-B. Son, I. Bloom, A. Dunlop, S. Trask *et al.*, *Energy Storage Materials*, 2021.

61 K.-H. Chen, M. J. Namkoong, V. Goel, C. Yang, S. Kazemiabnavi, S. Mortuza, E. Kazyak, J. Mazumder, K. Thornton, J. Sakamoto *et al.*, *Journal of Power Sources*, 2020, **471**, 228475.

62 C. Jin, T. Liu, O. Sheng, M. Li, T. Liu, Y. Yuan, J. Nai, Z. Ju, W. Zhang, Y. Liu *et al.*, *Nature Energy*, 2021, **6**, 378–387.

63 C. Cao, H.-G. Steinrück, P. P. Paul, A. R. Dunlop, S. E. Trask, A. N. Jansen, R. M. Kasse, V. Thampy, M. Yusuf, J. N. Weker *et al.*, *Journal of The Electrochemical Society*, 2022, **169**, 040540.

64 L. de Biasi, A. O. Kondrakov, H. Geßwein, T. Brezesinski, P. Hartmann and J. Janek, *The Journal of Physical Chemistry C*, 2017, **121**, 26163–26171.

65 O. Dolotko, A. Senyshyn, M. Mühlbauer, K. Nikolowski and H. Ehrenberg, *Journal of Power Sources*, 2014, **255**, 197–203.

66 T. M. Heenan, A. Wade, C. Tan, J. E. Parker, D. Matras, A. S. Leach, J. B. Robinson, A. Llewellyn, A. Dimitrijevic, R. Jervis *et al.*, *Advanced Energy Materials*, 2020, **10**, 2002655.

67 R. Xu, Y. Yang, F. Yin, P. Liu, P. Cloetens, Y. Liu, F. Lin and K. Zhao, *Journal of the Mechanics and Physics of Solids*, 2019, **129**, 160–183.